Laboratory scale geophysical measurements aimed at monitoring the thermal affected zone in Underground Thermal Energy Storage (UTES) applications

Laboratory scale geophysical measurements aimed at monitoring the thermal affected zone in Underground Thermal Energy Storage (UTES) applications.

N. Giordano[1], C. Comina[1-2], G. Mandrone[1-2]

[1] Earth Science Department – Torino University (IT), Via Valperga Caluso, 35 – 10125 Torino
[2] AG3 srl – A Spin Off Company of Torino University (IT), Via Valperga Caluso, 35 – 10125 Torino

Abstract

Underground Thermal Energy Storage systems have showed to be a useful and increasing technical solution for covering the heating and cooling and domestic hot water buildings' demand. Thermal influence of these plants is however not still debated as it deserves and correct monitoring strategies appear to be of major importance both to better understand processes and to highlight their environmental effects into high populated areas. Litho-, hydro- and bio-sphere can indeed be adversely affected by temperature variations induced in the underground by heat storage applications. For this purpose, a geophysical approach using time-lapse electrical resistivity measurements contemporary to analogical simulations is here tested at laboratory scale. Results of the experiments are reported comparing measured apparent resistivity with direct temperature measurements and numerical simulations of heat propagation. Data presented confirmed that electrical resistivity has powerful relation with temperature variation in monitored media. In addition, they showed that also without performing data inversion valid temperature estimation can be carried out. Post processing calibration of apparent resistivity data showed to be in acceptable agreement with both temperature measurements and numerical simulations. Simple apparent electrical resistivity variations appear therefore to be a promising, economic, quick and non-invasive tool for mapping thermal modifications induced in the underground by shallow geothermal applications.

Keywords: apparent electrical resistivity; numerical simulation; analogical modeling; porous media; shallow geothermal applications.

Corresponding author:
Nicolò Giordano
nicolo.giordano@unito.it
Dipartimento di Scienze della Terra
Via Valperga Caluso, 35
10125 – TORINO
tel. +39 011 6705325

1. INTRODUCTION

The idea of exploiting the thermal energy provided by renewable sources has been always related to the problem that most of these sources supply energy when the user's demand is low (e.g. sun energy is related to the warm season, when the heating demand is reduced). In this respect, the thermal energy storage is a highly debated concept since the late 70s; several Underground Thermal Energy Storage (UTES) technologies have been developed in recent years to find some new solutions assuring criteria of reliability, efficiency and economic sustainability. Short-term (daily) and long-term (seasonal) storages are the two main categories discriminating the storage mechanism, depending on the duration of the storing activity. The seasonal storage seems to satisfy the annual heat demand better than the short-term, with a 60% against a 20% of total energy demand provided (Fisch et al., 1998; Sanner, 2003; Xu et al., 2014). It is however true that the seasonal storage implies bigger economical investments and wider storage volumes, hence it results in a more challenging technology in terms of storing materials, heat loss evaluations and environmental impact reductions.

UTES systems are based on the sensible heat storage mechanism which is considered to be a simple, low-cost, more reliable and acceptable technology compared to other alternatives (latent heat or chemical reaction/thermo-chemical sorption), even if the latter have higher energy storage densities (for detailed discussion refer to Xu el al., 2014). Several methodologies are available depending on the storing medium: (ATES – Aquifer Thermal Energy Storage) (Rosen, 1999; Paskoy et al., 2000; Dickinson et al., 2009), hot water confined in steel tanks (Novo et al., 2010; Schmidt et al., 2004) or the ground itself; in this last case the connection with the ground is provided by a series of boreholes heat exchangers (BTES – Boreholes Thermal Energy Storage) (Bakema et al., 1995; Fisch et al., 1998; Reuss et al., 2006; DLSC, 2012; Giordano et al., 2016).

Mainly ATES and BTES have therefore geological implications. In both cases, thermal and hydrogeological properties of the ground have to be taken into account for the design and operation of the installation. Both storage systems have a strong environmental impact: a big part of the aquifer could be influenced in the first case, a noticeable underground volume is interested by drilling activity in the latter. In any case a not negligible Thermal Affected Zone (TAZ) is generated and an accurate monitoring activity must be considered to take care of the possible negative effects induced on litho-, hydro- and bio-sphere. Generally, an accurate study of the thermal behavior of the storage medium and a correct monitoring of TAZ are also useful to understand processes.

So far, there is limited specific knowledge about the effects of unsuitable system design (e.g. unwanted temperature and chemical changes within the subsurface and resulting consequences). Only few studies have measured the thermal effects of low enthalpy geothermal applications within field sites. Arslan and Huber (2013) compared field temperature observations with numerical simulations and laboratory measurements under a forced groundwater flow. Lo Russo et al. (2014), evidenced that the thermal plumes generated by well doublets of groundwater heat pumps can be regarded either as a potential resource or as a pollution. Bonte (2013) studied temperature-induced impacts on the groundwater quality, accounting for variations in the mobility of trace elements, redox processes and microbial communities. Most studies agree that a 10°C temperature change can be sufficient to stimulate trace elements mobility and microbial activity variations. Considering high temperature (60°C – 70°C) fluids injected in the ground by energy storage systems a potential environmental impact has therefore to be considered.

Classic thermal tests or monitoring strategies often rely on local and point-based measurements to monitor changes in temperature. In this context, geophysics can bring complementary information which is spatially distributed and acquired directly from the ground surface. In particular, electrical resistivity measurements could be considered as a time and cost-efficient method for monitoring shallow geothermal systems to understand thermal processes. Hermans et al. (2015) demonstrated the ability of cross-borehole time-lapse resistivity tomography to study heat flow and heat storage within a small field experiment in a shallow aquifer and Hermans et al. (2012) successfully used surface resistivity measurements to monitor temperature variations. Fragkogiannis et al. (2008) also used resistivity tomography for monitoring the thermal performance of an installed ground source heat pump system. Robert et al. (2013), under laboratory conditions, highlighted the problems of resistivity-derived temperatures owing to chemical reactions occurring both on fluid and solid phases. They observed a divergence between resistivity and temperature curves, related to decreasing solubility of some minerals (e.g. calcite precipitation) and resulting decreasing fluid conductivity with increasing temperature. A more detailed review on the use of geophysical methods to monitor temperature changes induced in the underground by shallow geothermal systems can be found in Hermans et al. (2014). More case studies are also provided by Arato et al. (2015).

Resistivity based measurements are potentially very powerful since useful relationships can be found in literature between temperature and electrical resistivity (Campbell, 1948; Lee and Deming, 1998; Fragkogiannis et al., 2008; Rein et al., 2004; Hayashi, 2004; Hayley et al., 2007). However, resistivity depends also in a complex way on different soil and environmental attributes. Friedman (2005) gave an overview of these parameters, and their impact, underlining three categories: (i) parameters describing the bulk soil, such as porosity (Φ), water content (θ) and structure; (ii) the time-invariable solid particle quantifiers, such as particle shape and orientation, particle-size distribution, wettability or cation exchange capacity; (iii) fast-changing environmental factors, such as ionic strength, cation composition and, finally, temperature. A proper, but not easy, parameter calibration should be undertaken in order to infer relevant information such as the extension of TAZ. Devoted tests are therefore necessary in this respect. As an example, laboratory tests have the advantage that controlled boundary conditions can be obtained (parameters from the first and the second groups) such that a direct comparison of geophysical results, temperature measurements and numerical simulations can be performed. After a proper calibration it will be then possible to use electric resistivity variations with time as an imaging tool for the distribution of thermal plumes. This approach can be also profitably extended at the field scale, if some of the mentioned parameters do not change during time (particle size distribution, water content, porosity etc.).

The present paper therefore presents a series of laboratory tests performed on an *ad hoc* designed apparatus for testing and calibrating a methodology for monitoring the extension of TAZ caused by underground storage applications. A heat injection was induced in a porous medium and time-lapse electrical measurements were carried out together with local temperature measurements and a Finite Element Method (FEM) numerical simulation of the heat propagation. Several tests were performed by varying: porous medium, position and number of heat sources, hydraulic conditions and injection time. Resistivity and temperature measurements were then compared with numerical simulations to estimate the reliability of apparent resistivity variations in qualitatively mapping TAZ extension within the medium and in quantitatively evaluating temperature distribution within it.

2. MATERIALS AND METHODS

The proposed testing methodology consists of the following steps:

- Analogical test: heat injection and heat turnoff monitored by 4 temperature sensors located in the medium and by hourly electrical measurements in spatial arrangement, on two different media;
- Numerical simulations: numerical modeling of heat propagation calibrated on local temperature measurements to extend temperature information spatially end evaluate the eventual differences in homogeneous parameters variation;
- Resistivity data processing: calibration of the fractional change in electrical resistivity based on the comparison with local resistivity data and temperature measurements;
- Temperature prediction and comparison: imaging of the resistivity-derived temperature maps by means of the previous step and comparison with the numerical simulations.

Details on the instrumentation and procedures adopted in each step are provided in the following.

2.1 Laboratory apparatus and performed tests

A plastic box, sized 0.8 x 0.3 x 0.3 m (**Fig. 1**), was prepared to simulate a heat injection within the selected porous medium. Three sectors separated by permeable septa were predisposed in order to focus the simulation in the central part of the box. In the external sectors two PVC pipes, surrounded by a high porosity filling material, were placed for generating a water flux by controlling the hydraulic head in the pipes. The central sector, about 0.6 m long, was filled with a porous medium for 0.3 m of thickness and was equipped with 4 thermo-resistances Pt100 (accuracy ± 1°C, resolution 0.2°C), located at different positions depending on the test, for the temperature monitoring. An electrical resistance (diameter 4 cm) and powered by alternated current was used as heat source. During the tests, the source was controlled by a thermometer and a rheostat, to assure desired constant temperature (60°C for all the tests). For one of the presented tests a double source has been used (**Tab. 1**). The boundaries of the box where thermally insulated using cork panels and impermeable membranes. A data-logger and appropriate software were used for data acquisition, in order to register continuously all the controlling parameters (sampling interval 1 minute).

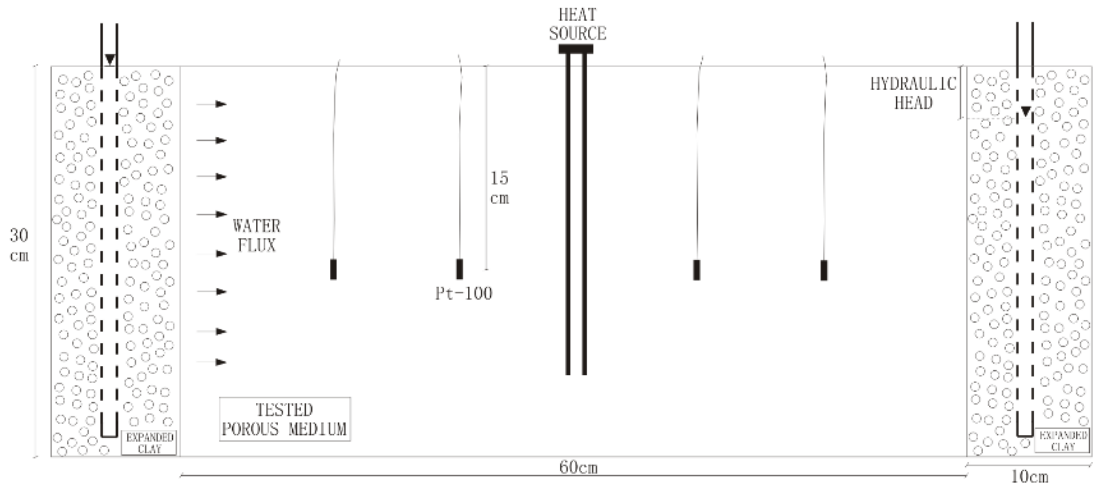

Fig. 1. Schematic depiction of the laboratory device used for the experimental tests.

Tab. 1 – Summary of the presented tests

Name	Porous medium	Water flux [l s^{-1}]	Processes	Heat injection	Source position
Fs	Fine	-	Conduction	9 h	1 source central position
Fd	Fine	$1.5x10^{-3}$	Conduction & convection	5 h	1 source central position
Cs	Coarse	-	Conduction	5 h	2 sources left side
Cd	Coarse	$3.0x10^{-3}$	Conduction & convection	5 h	1 source central position

A network configuration with 24 electrodes (6 lines of 9 cm spaced electrodes) was adopted to achieve a wide spatial information around the sources (**Fig. 2**). A SYSCAL Pro multichannel georesistivimeter was used for resistivity measurements. A short current injection time (250 ms) was adopted in order to record the set of measurements as quick as possible. A dipole - dipole array with 36 measurements (plus reciprocal, for a total of 72 measurements) was adopted. This configuration allowed us to record resistivity values roughly at the same depth of temperature sensors and to image its variation during time in a plan view around the heat source. Dipole - dipole configuration was adopted in order to improve data coverage, since number of electrodes and available space are reduced. This situation often affects also real site data, particularly in urban environment. Moreover, dipole - dipole is more prone to evaluate lateral variation in resistivity as in the case for an advancing thermal plume. Midpoints of dipole - dipole measurements are reported in red in **Fig. 2**.

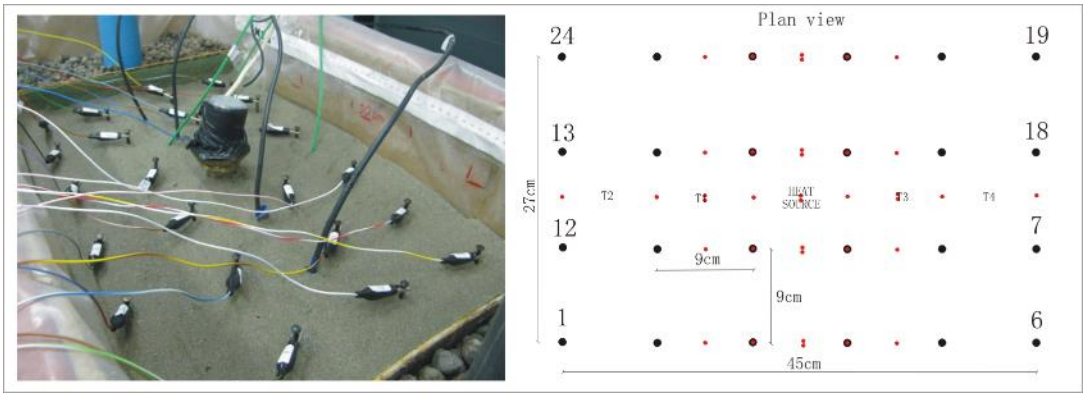

Fig. 2. Electrode configuration adopted in the tests with dipole-dipole centre location (red dots on the right); the picture and the position of the temperature sensors refer to Fs test.

Two natural porous media with different grain size distributions were adopted. These materials come from two quarries nearby Torino and are therefore intended to represent typical local geological conditions of the municipality. The two media were respectively made of: (i) a fine medium with 91% wg. of sand and 9% wg. of silt, compacted at a porosity of 0.46; (ii) a coarse medium with 58% wg. of gravel (mean particle diameter d_0 = 5-6 mm) and 42% wg. of sand, compacted at a porosity of 0.35. In the present paper 4 examples of several tests conducted in the box are presented (**Tab. 1**). The tests are intended to simulate the heat injection under realistic conditions; in one of the tests a double injecting source was also used. In both media a pure conduction test, with the medium completely saturated by tap water, and a conduction + convection test, where a water flux was simulated by inducing a hydraulic head gap between the two side of the box are presented. A flow rate of about 3.0 x 10^{-3} l/s of water at room temperature was induced in the coarser medium, while the flow rate adopted in the finer was about 1.5 x 10^{-3} l/s, owing to the different permeability coefficients of the tested media. The tests lasted at least 10 hours, with 5 hours of heat injection and the remaining 5 hours of cool

down. The electrical surveys were performed hourly from the beginning (zero condition) until the end of the tests, when the undisturbed temperature was reached again.

2.2 Numerical simulations

To simulate the heat injection within the medium, the OpenGeoSys code (OGS) was adopted (Kolditz et al., 2012). OpenGeoSys is an open-source initiative for the numerical simulation of thermo-hydro-mechanical/chemical processes. It is a flexible FEM numerical framework, provided to solve multifield problems in porous and fractured media for several geological and hydrological applications. The simulations were performed using the *heat_transport* process for the static tests and the coupled *heat_transport* and *groundwater_flow* processes for the tests simulating coupled conduction and forced convection phenomena. The OGS governing equations for both "pure conduction" heat transport and "conduction + convection" heat transport can be summarized in the energy balance equation, taking into account every element of the bi-component medium (solid and water):

$$\gamma_b C_b \frac{\partial T}{\partial t} + \nabla \mathrm{q}_T = Q_T \quad [1]$$

where at the first member the temperature (T) variation as a function of time multiplied by density (γ_b) and specific heat capacity (C_b) of the medium are summed to the heat flux term q_T, which can be divided in the two components of advective and conductive flux as follows:

$$\mathrm{q}_T = \Phi\theta\gamma_w C_w \mathrm{v}T - \lambda_b \nabla T \quad [2]$$

where Φ is the porosity, θ the water content, γ_w and C_w the density and the specific heat capacity of water, v denotes Darcy velocity and λ_b is the bulk thermal conductivity.

Some preliminary evaluations comparing *ad hoc* simulations with available analytical solutions and experimental tests were used to calibrate geometric elements, discretization mesh, Dirichlet and Neumann boundary conditions, time step definition, medium, material and fluid properties. The simulations were carried out setting up the same characteristics of each experimental test performed at lab scale. A 3D model with a rectangular prism mesh of about 75,000 nodes was adopted. Lateral sides of the box were simulated as impermeable boundaries, not allowing for heat or fluid flow and only the upper boundary was a diffusing one. The finally adopted physical properties of the tested materials are presented in **Tab. 2**.

Tab. 2 – Physical properties of the tested media adopted for numerical simulations.

	Φ	**γb** [t m^{-3}]	**ki** [m^2]	**λs** [W m^{-1} K^{-1}]	**λw** [W m^{-1} K^{-1}]	**Cs** [J kg^{-1} K^{-1}]	**Cw** [J kg^{-1} K^{-1}]	**Δi** [m]
Fine medium	0.46	1.47	1x10^{-11}	5.0	0.58	800	4,200	0.05
Coarse medium	0.35	1.72	3x10^{-11}	5.0	0.58	800	4,200	0.05

2.3 Electrical resistivity vs. temperature

2.3.1 Adopted methodology

A linear dependence between temperature and electrical conductivity (σ – the inverse of resistivity) can be assumed in the temperature range in question (Hermans et al., 2012). Around 25 °C the following relation has been proposed:

$$\frac{\sigma_T}{\sigma_{25}} = m(T - 25) + 1 \quad [3]$$

where σ_T is the electric conductivity of the porous medium at temperature T (°C) and m is the fractional change in electrical conductivity (°C^{-1}). A range of 0.018 °C^{-1} and 0.025 °C^{-1} has been found by several authors for m (Revil et al., 1998; Hayashi, 2004; Hayley et al., 2007; Hermans et al., 2012) and it varies according to the type of fluid and sediments. Water and surface conductivity effects can be separated in case of a silty or clayey medium, accounting for different fractional changes, m^f for fluid and m^s for surface conductivity. According to Revil and Linde (2006) the surface conductivity is related with the average particle diameter of the medium as follows:

$$\sigma_S = \frac{6\Sigma_S}{d_0} \quad [4]$$

where Σ_S is the specific surface conductivity (S) and d_0 is the mean particle diameter. If we reasonably assume the specific surface conductivity equal to 4.0 x 10^{-9} S (Bolève et al., 2007), we obtain σ_S = 1.6 x 10^{-4} S/m and σ_S = 9.6 x 10^{-6} S/m respectively for the finer (d_0 = 0.15 mm) and the coarser media (d_0 = 2.5 mm). By considering that the applied tap water conductivity is 5.0 x 10^{-2} S/m, we can thus neglect the surface conductivity effect in the performed tests and assume the bulk electrical resistivity variation during the heat injection completely related to the water contribution. At the same time the reduced testing time allows also assuming constant values for ionic strength and cation composition. These assumptions hold for the clay-free materials under study and for limited heating time and may not be completely applicable in the presence of high concentrations of carbonates.

We have now to transform **Eq. [3]** for the purposes of this study, and so to obtain a relationship between temperature and apparent resistivity variation. By considering σ_{25} as the reference value at the initial conditions, σ_T the value at a defined step during the test and by transforming the equation in terms of apparent resistivity we thus obtain:

$$\frac{\rho_{a_0}}{\rho_{a_t}} = m(T_t - T_0) + 1 \quad [5]$$

where ρ_{a0} is the apparent resistivity at zero condition (before the starting of the heat injection), ρ_{at} is the apparent resistivity measured at a defined step, T_0 and T_t are temperature at the respective time. From **Eq. [5]** we can obtain:

$$\Delta\rho(\%) = \frac{100}{m\,\Delta T + 1} - 100 \quad [6]$$

which relates apparent resistivity variation in percentage $\Delta\rho_a(\%)$ from zero condition to the difference in temperature ΔT, always depending on the fractional change in resistivity which is medium-dependent. With **Eq. [6]** we are able to predict the variation in resistivity by knowing the increase or the decrease in temperature induced in the tested medium. Analogously, by inverting the proposed relation in terms of temperature it is also possible to predict the temperature distribution within the medium by performing time-lapse electrical resistivity measurements, **Eq. [7]**:

$$T_t = \frac{1}{m}\left(\frac{100}{\Delta\rho_a(\%)+100} - 1\right) + T_0 \quad [7]$$

In our approach, we used apparent resistivities avoiding data inversion for several motivations:

- given the almost homogeneous condition of the tested materials, measured apparent resistivities can be quite reasonably approximated to the true resistivity of the medium;
- it is well known that inversion can introduce unwanted artifacts that may bias the results and interpretation particularly on sparse data;
- the limited number of electrodes (space requirements) and the few measurements performed did not provide enough data to allow for a rigorous inversion;
- on a complementary side, few electrodes and short current injection time is necessary for an acquisition time comparable to the monitored phenomenon and it is the most common situation in real sites with limited space;
- last but not least, we wanted to test a fast and simple methodology that could be potentially applied on site for monitoring purposes, at least in favorable sites (i.e. characterized by nearly homogeneous conditions), avoiding too much data elaboration.

Apparent resistivities were obtained from measured resistances by adopting a standard geometric factor (*k*) for dipole - dipole array over infinite homogeneous half-space. To ensure the reliability of this operation if compared to the limited dimensions of the box, forward model simulations were carried out with R3t code (Prof. Andrew Binley, © 2012, Lancaster University), considering the presence of insulating boundaries, in order to estimate *k* factor's differences with respect to homogeneous half-space. Changes in geometrical factor greater than 15% were observed only close to the boarders of the box, while divergences in the center are less than 10% and comparable to measurements' errors (see after). It has moreover to be considered that data processing was performed with time-lapse differences with respect to starting conditions; this procedure helps to eliminate the influence of the box's walls on the apparent resistivity changes observed, being constant the effect on electric current paths during the tests.

2.3.2 Data error analysis

As before mentioned, both normal and reciprocal resistance measurements were acquired. Together with repeatability tests, reciprocal error quantification can be adopted as a measure of noise in order to prevent misinterpretation of ERT images (Slater et al., 2000). In the present study, repeatability tests were not performed because as fast as possible resistivity measurements were needed. Only reciprocal errors were quantified and analyzed in order to evaluate reliability of the measurements. Reciprocal error known as $E_{N/R}$ (LaBrecque et al., 1996) can be achieved by:

$$|E_{N/R}| = R_n - R_r \quad \text{Eq. [8]}$$

where R_n and R_r are resistances measured by normal and reciprocal quadrupoles respectively. Since for the principle of reciprocity exchanging current and potential electrodes should not change measured resistance, reciprocal error gives a measure of data noise.

$E_{N/R}$ of each measurement step during heat injection tests were plotted against resistance data *R* (average between normal and reciprocal) and an error envelope given by:

$$|E_{N/R}| = a + b \cdot |R| \quad \text{Eq. [9]}$$

with $a = 0.4$ and $b = 0.02$, encompassed almost the totality of data in each test. As showed in **Fig. 3**, Cd is the worst test, with 6-7 outliers but only 1 of them with error greater than 10%, which is typically adopted as threshold (Slater et al., 2000). We therefore decided to keep all data sets in each experiment here presented, because even if erasing outliers could bring to better apparent resistivity estimation, it is however true that an artificial kriging interpolation obtained by voids in the measurements can bring to exaggerated smoothing or artificial imaging in the 2D maps. In this case, where only few measurement points are available (owing to above mentioned reasons), it was decided to keep all the data but being aware of reciprocal error distribution during data interpretation. Again, working with time-lapse differences can lower the influence of this error on data processing; indeed, in the performed evaluations $E_{N/R}$ was observed to remain almost constant during the whole duration of the tests.

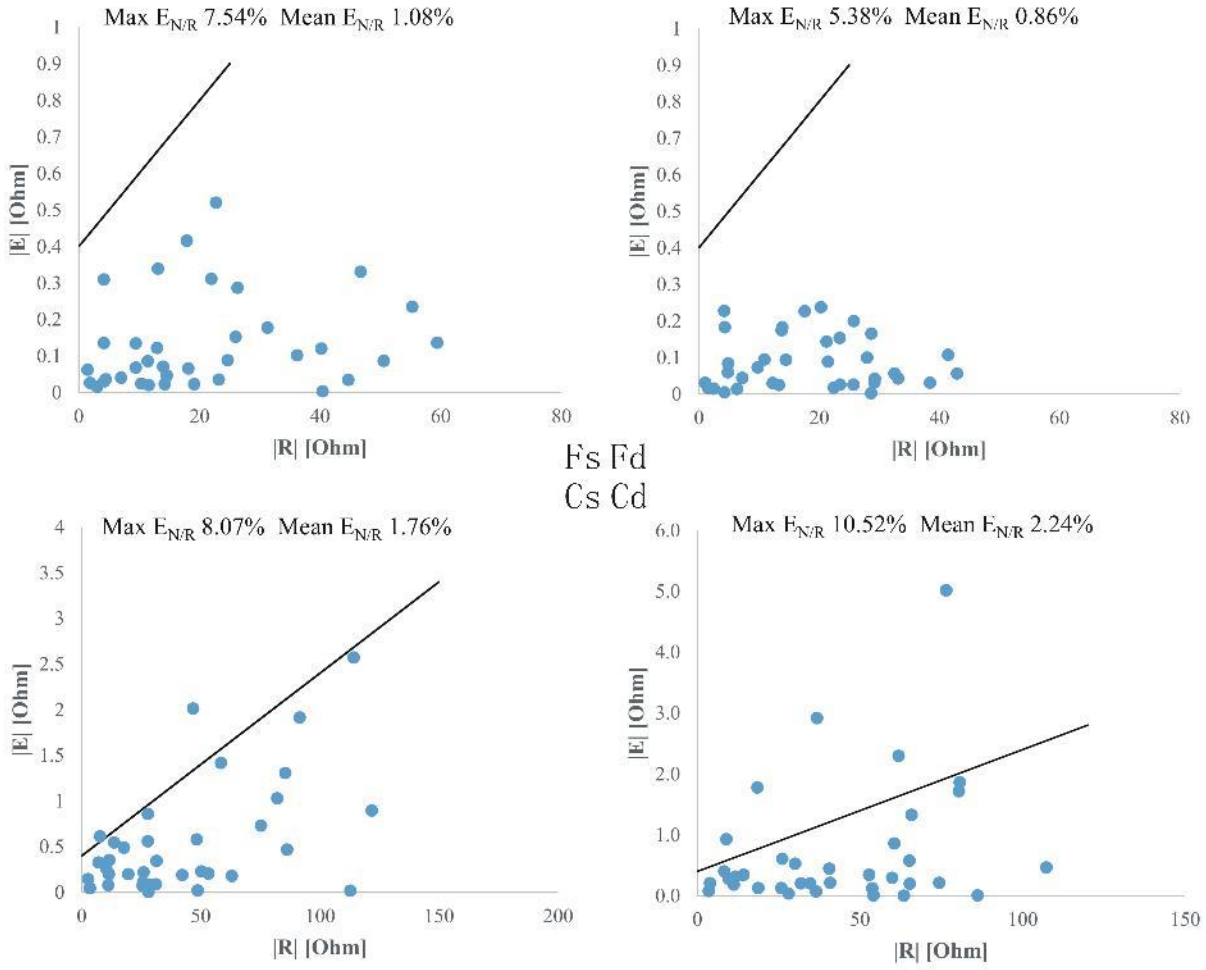

Fig. 3. Reciprocal error |E| plotted against average resistance values |R| for the zero condition (before heat injection started) of each test. Black lines are the error envelope with a = 0.4 and b = 0.02. Maximum and mean reciprocal errors of each test are also reported.

3. RESULTS

The results of the numerical simulations in each of the 4 tests compared with the temperature experimental data are reported in **Fig. 4** (for reference to the location of temperature sensors refer to **Figs. 6-9**). In **Tab. 3**, the misfit of numerical versus experimental temperatures are reported. It can be observed that a valid match was reached in most of the tests allowing for the reconstruction of the full temperature field inside the box. Particularly the average misfit values remained below 3.5 % for all the tests apart the one under static water condition on the fine material (Fs test) which indeed show an increased average uncertainty. This test is also the one having the longer injection time causing possible evaporation phenomena as will be discussed in section 4.

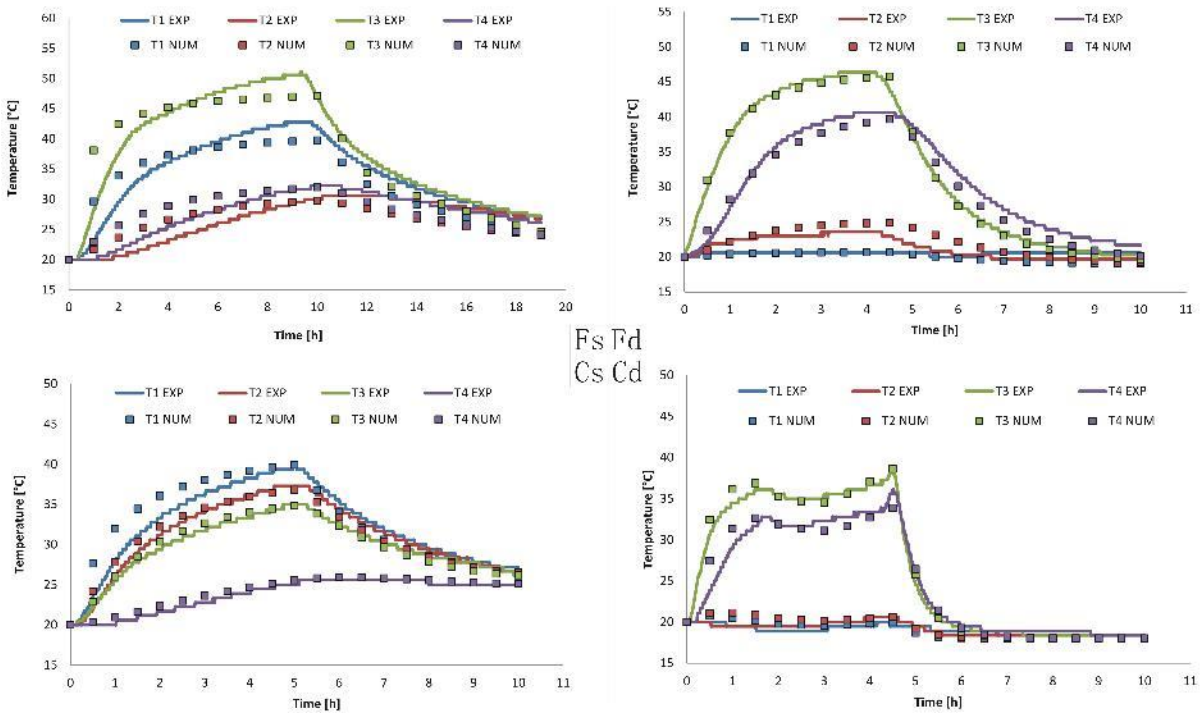

Fig. 4. Comparison between measured (continuous curves) and numerical (dotted curves) temperature data in all the tests. In the Fs test, T2 and T1 were 15 and 8 cm upline of the source, while T3 and T4 were downstream at 5 and 15 cm respectively. For the Fd and Cd tests T1, T2 and T3 were placed at about 10 cm around the source, while T4 was at 20 cm. In the Cs test T1, T2 and T3 were placed at 8 from one of the sources, while T4 was at 20 cm; the OGS numerical simulation also managed to represent the unwanted temperature decrease at the source during the Cd test.

Tab. 3 – Average temperature divergences between numeric and experimental data of Fig. 3 (absolute values in %). Steps from 1 to 5 and from 6 to 10 refers respectively to heat up and cool down.

Test	1	2	3	4	5	6	7	8	9	10	Average
Fs	13.06	7.65	4.96	4.55	1.84	7.63	9.02	8.84	9.44	9.90	7.69
Fd	1.61	1.86	1.96	2.59	4.36	4.39	4.88	4.05	4.68	5.47	3.59
Cs	6.33	4.22	3.41	1.63	1.02	2.37	2.42	3.13	2.50	1.47	2.85
Cd	6.26	2.86	3.47	1.38	3.53	2.73	3.10	2.71	2.07	2.10	3.02

The flowing water test on the coarse material (Cd test) showed the smallest peak temperature because of the high velocity of the induced flux, which did not allow the water to

heat up the medium properly. Contrary to the other ones this test do not present big variations between the first and the last hour of the heating period. The hydraulic flux warmed up the medium more rapidly, reaching the temperature peak within the first hour. Moreover, after the peak, an unexpected temperature decrease in the heat injection during the test (from 60 °C to 50 °C from hour 1.5 to hour 3) was recorded. This effect was taken into account in the simulations. The analogous test in the fine medium is instead characterized by curves shaped similarly to stationary tests (Fs and Cs) due to the slower flow velocity. The flux velocity plays therefore a major role in transporting the heat. Among all the tests, those performed in the fine medium reached the biggest temperature peaks. A finer material is more able to limit the heat losses than a coarser one. These losses are mainly ascribable to the pore-filling water, which is obviously less constrained by the capillary pressure in a coarser than in a finer medium.

Fig. 5 shows the comparison between the temperature recorded by the 4 sensors during the tests (for reference in the location of temperature sensors refer to **Figs. 6-9**) and the resistivity-derived temperature obtained by applying **Eq. [7]** to the local resistivity measurements nearby the sensors. Best fit *m* values of 0.025 $°C^{-1}$, for the finer medium, and of 0.021 $°C^{-1}$, for the coarser medium were obtained, reaching again a valid match both in static and in dynamic conditions. The temperature-sensitivity of resistivity data is particularly clear in the test on the coarse material (Cd test): resistivity data are indeed able to reflect the temperature trend during heating related to the decrease in temperature of the source. In the cooling periods a divergence between temperature and resistivity-derived data is highlighted in Fs and Cd tests. In the first case the resistivity-derived temperature shows a slower return to the initial conditions with respect to T-sensor recordings, in the second case the opposite is true. In **Tab. 4** the misfit of resistivity-derived versus experimental temperatures are reported. A valid agreement can be particularly noted in all the heating periods with an average misfit below 5%. In Fs and Cd tests an increase in the average misfit (particularly high for the Cd test) is observed. Motivations for this divergence will be discussed in Section 4.

Tab. 4 – Average temperature divergences between resistivity-derived and experimental data of Fig. 4 (absolute values in %). Steps from 1 to 5 and from 6 to 10 refers respectively to heat up and cool down.

Test	1	2	3	4	5	6	7	8	9	10	Average
Fs	7.62	4.96	4.41	4.52	4.05	1.62	4.62	6.47	8.40	9.36	5.60
Fd	3.30	3.46	3.64	3.43	5.33	7.13	3.61	2.77	3.10	2.84	3.86
Cs	5.74	2.58	1.59	1.21	1.61	2.24	2.21	4.85	3.26	4.91	3.02
Cd	11.05	13.15	13.26	11.01	11.35	20.49	20.07	23.34	23.75	24.60	17.21

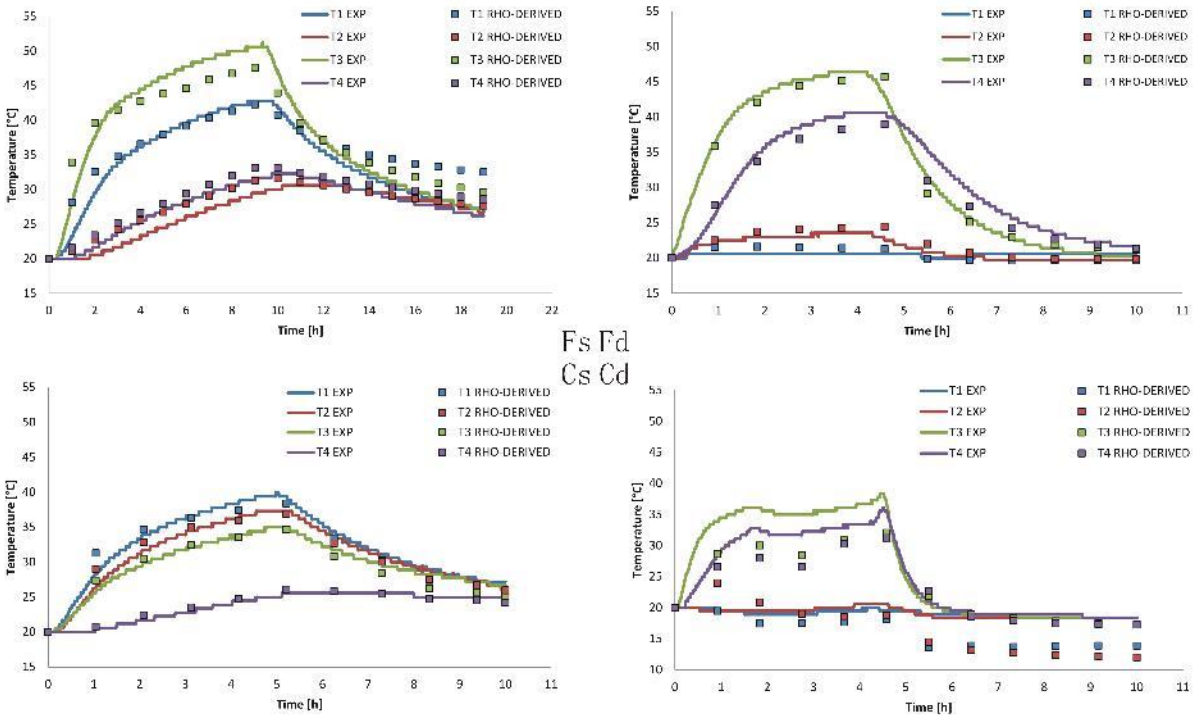

Fig. 5. Comparison between measured (continuous curves) and resistivity-derived (dotted curves) temperature data in all the tests. The latter are calculated with Eq. [7] from the resistivity data registered by quadrupoles just around the sensors.

Finally, **Figs. 6, 7, 8** and **9** present the comparison between numerically modelled and resistivity-derived temperatures in all the tests in a 2D representation. These maps were obtained with a Kriging interpolation of the temperature values deduced by apparent resistivity variation. Kriging method was applied accounting for the analysis of the spatial data variability; in each test, best fit of experimental variograms was found to be a linear variogram model in every time step. Apparent resistivity monitoring highlighted its potentiality in describing the heat diffusion from the source in all the tests. In the Fs test (**Fig. 6**), which is the longest among all the performed tests, temperature maps near the peak are not so homogeneous and also the cooling down shows some portions where the resistivity is higher (white portions above and below the source) and other parts where instead a lower resistivity generated a higher temperature estimation. The experiment with flowing water in the fine medium (Fd, **Fig. 7**) shows a good agreement throughout the whole testing time. The left portion of the maps remained at an almost constant temperature for the entire heating period, while the right portion is validly described by the resistivity monitoring, except for some heterogeneities just around the source. The Cs is the best example among all (**Fig. 8)**: the heating period is in valid accordance with the peak temperatures and the shape of the heated plume (caused by the presence of two heating sources); the cooling down is also correctly described by the resistivity monitoring. The flowing water test on the coarse material (Cd, **Fig. 9**) shows the ability of the electrical surveys to qualitatively describe the migration of the heated plume due to the water flux. The heating predominant in the right portion of the box is clearly highlighted. The quantitative representation of the temperature field is however not effective as already commented in relation to **Fig. 5**. The discrepancy of the resistivity derived maps from the homogeneous reference condition of numerical simulations (particularly **Figs. 6** and **9**) is however not surprising since probable different effects could be present. Again, motivations for the evidenced discrepancies will be commented in Section 4.

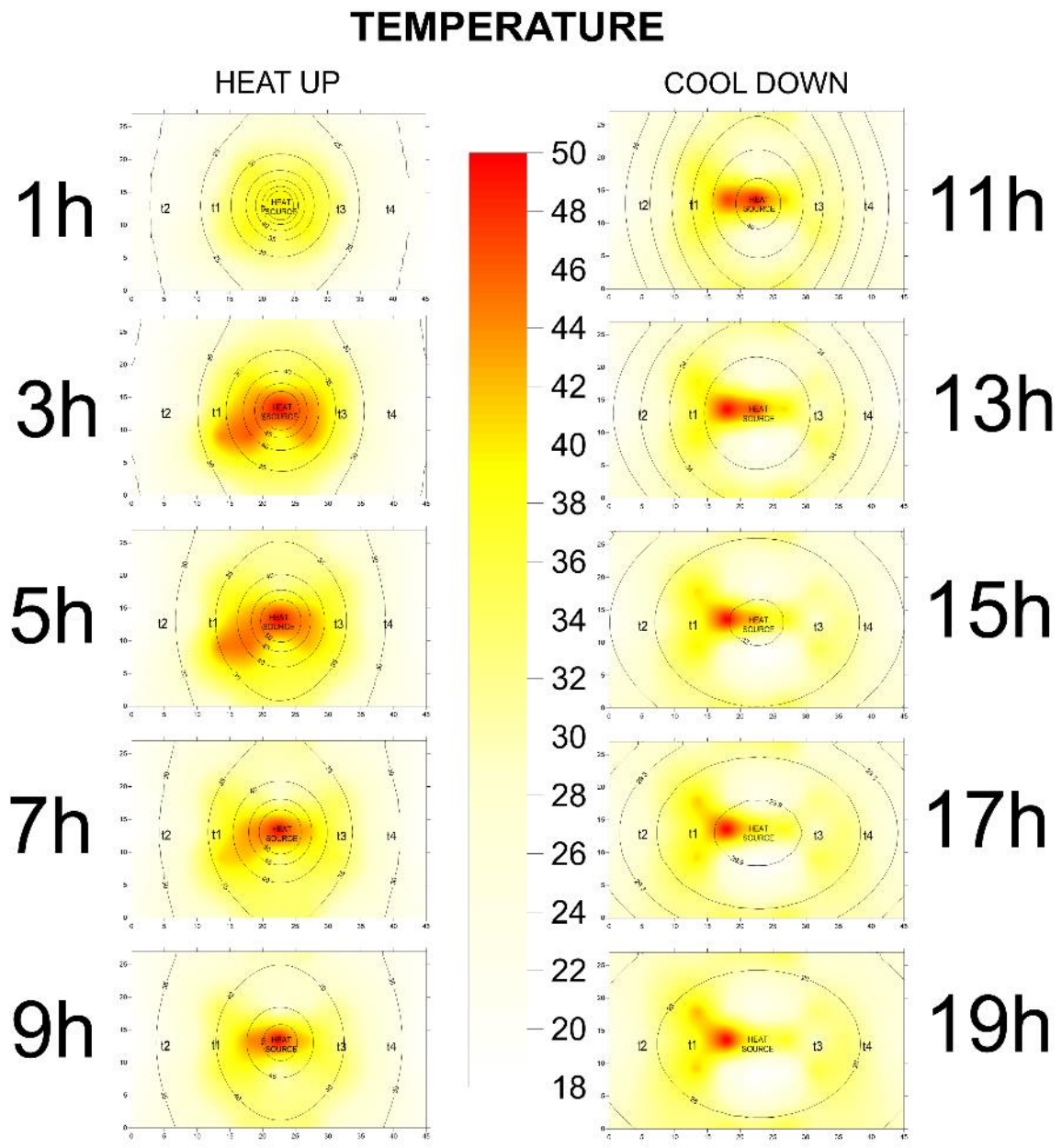

428

429 **Fig. 6.** Comparison between numerical (contours) and resistivity-derived (colored maps) temperature data in the
430 Fs test. The numerical temperature is provided by the OGS simulation calibrated on the temperature recorded by
431 each sensor. The resistivity-derived temperature is obtained by Kriging local resistivity transformed data.

432

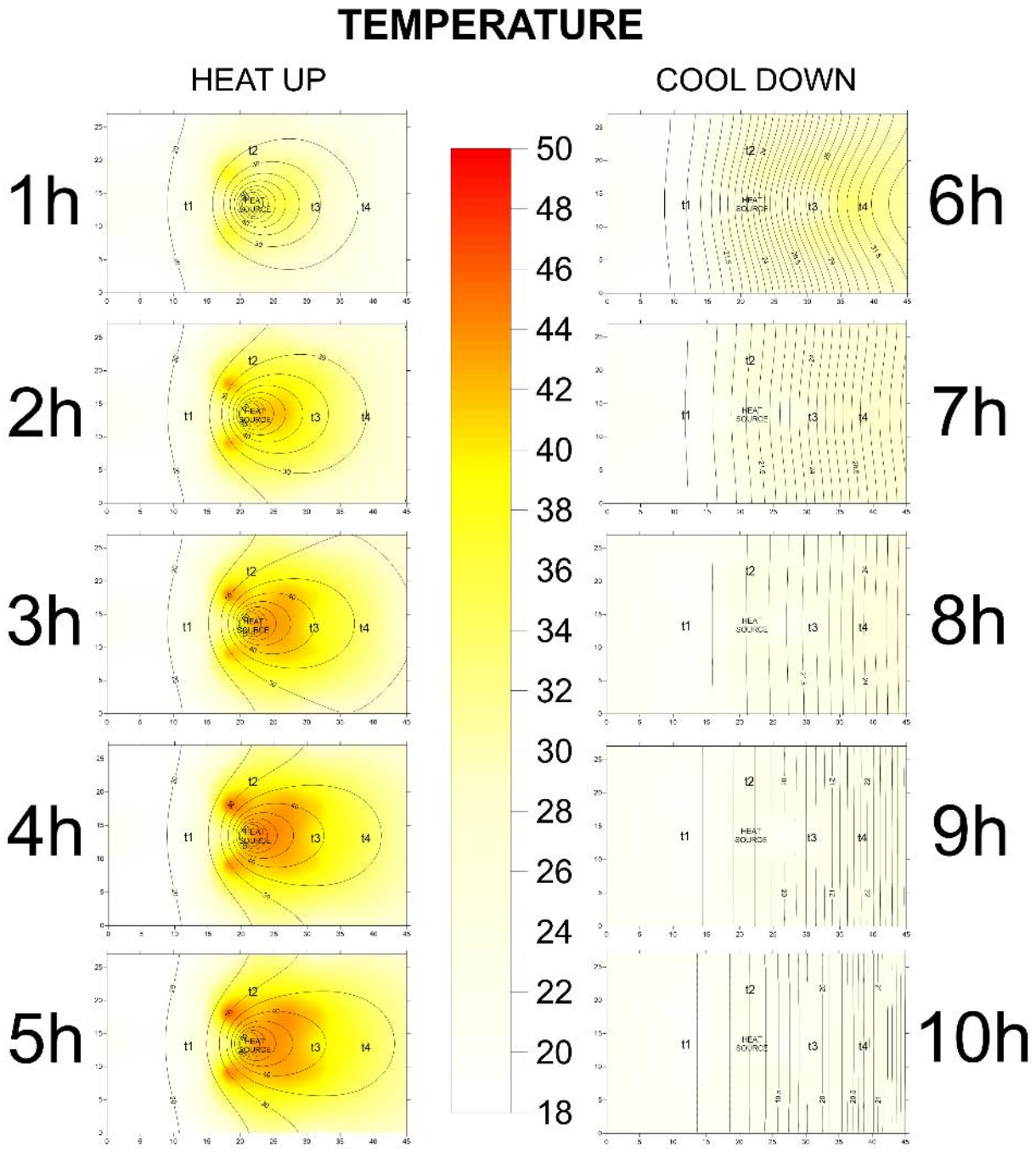

Fig. 7. Comparison between numerical (contours) and resistivity-derived (colored maps) temperature data in the Fd test. The numerical temperature is provided by the OGS simulation calibrated on the temperature recorded by each sensor. The resistivity-derived temperature is obtained by Kriging local resistivity transformed data.

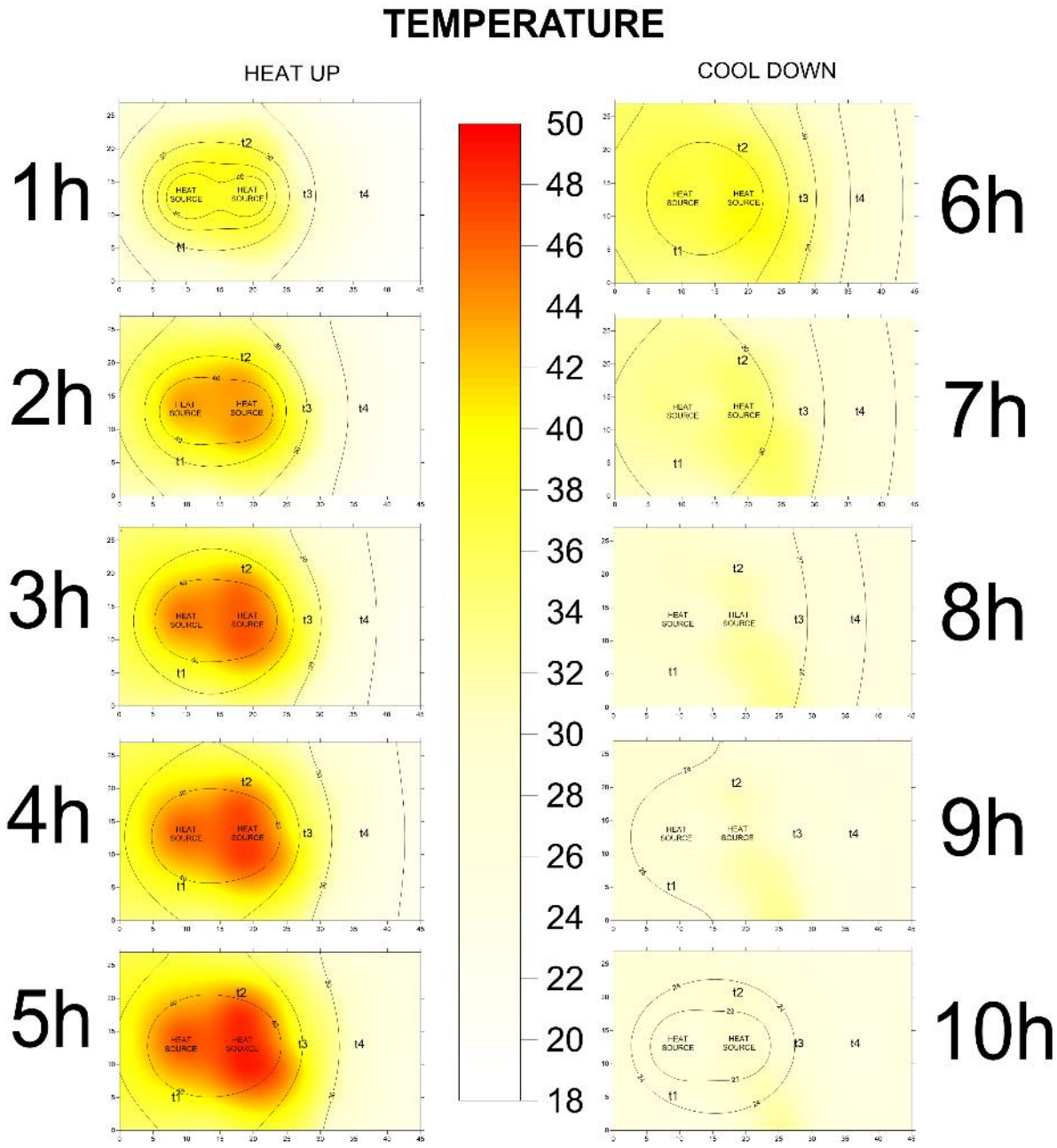

Fig. 8. Comparison between numerical (contours) and resistivity-derived (colored maps) temperature data in the Cs test. The numerical temperature is provided by the OGS simulation calibrated on the temperature recorded by each sensor. The resistivity-derived temperature is obtained by Kriging local resistivity transformed data.

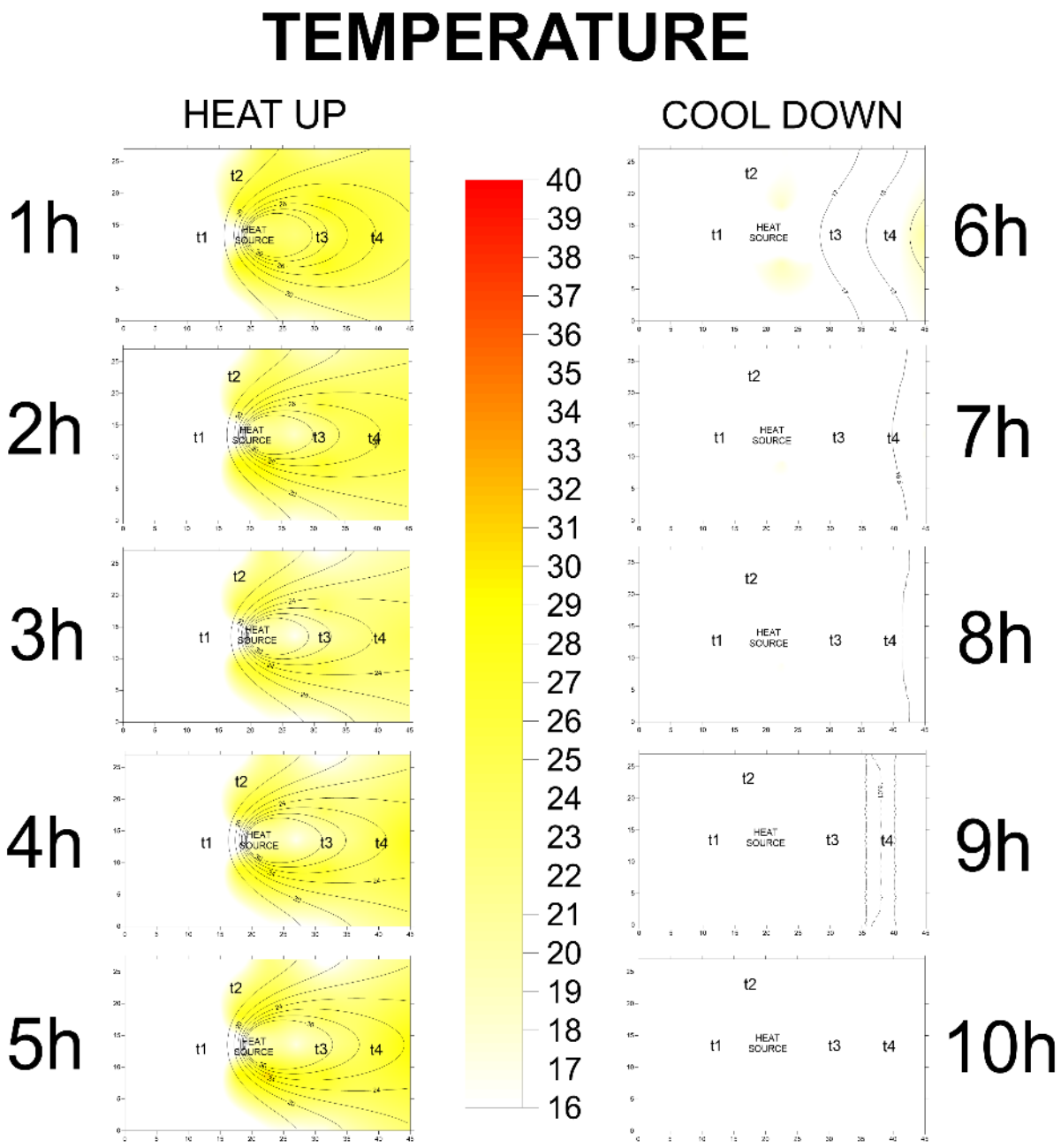

Fig. 9. Comparison between numerical (contours) and resistivity-derived (colored maps) temperature data in the Cd test. The numerical temperature is provided by the OGS simulation calibrated on the temperature recorded by each sensor. The resistivity-derived temperature is obtained by Kriging local resistivity transformed data.

For quantitatively evaluate the fit of the resistivity estimated temperatures, each resistivity-derived temperature map was compared with the numerical one at each time step. The average of the divergences for each time step is reported in **Tab. 5**. Generally an overestimation trend was always observed. Fs, Fd and Cs tests stand at an acceptable bias of 10 ± 2%, while Cd shows worse values, as expected. Among all the tests, in the Cs experiment the best agreement was found, confirming the effective temperature estimate shown in the above reported figures. Conversely to the others, the Cs bias decreases when approaching the peak of the heat injection, reaching the smallest value 1 h after the source's turning off. **Fig. 10** reports a comparison between the numerical and the resistivity-derived TAZ. This can better help in evaluating the potentiality of the resistivity monitoring for imaging the extension of the thermal plume. Fs, Fd and Cs show a valid agreement with a little overestimation particularly in the higher isotherm (40°C). Cd test is clearly more disturbed than the others. In general, it can be

said that the resistivity measurements performed during the heat injection described the TAZ induced in the medium with an acceptable misfit and that the little overestimation of their extension can be seen as conservative.

Tab. 5 – Average temperature divergences between numeric and resistivity-derived data of Figs from 5 to 8 (absolute value in %). Steps from 1 to 5 and from 6 to 10 refers respectively to heat up and cool down.

Test	1	2	3	4	5	6	7	8	9	10	Average
Fs	9.86	11.16	12.10	14.78	13.87	10.42	11.20	12.21	13.41	14.80	12.38
Fd	10.78	11.56	11.71	11.86	12.40	7.14	6.84	6.61	7.93	7.79	9.46
Cs	10.09	7.61	7.27	7.13	7.32	6.14	6.29	6.59	8.94	12.64	8.00
Cd	25.23	26.01	28.05	29.43	29.78	28.04	37.89	39.78	41.03	41.54	32.68

4. DISCUSSION

The numerical modeling was useful to obtain a reference temperature distribution within the medium. The 4 time-lapse local temperature curves registered by the sensors were not sufficient alone to interpolate the induced thermal plume throughout the medium This is a common problem when local temperature monitoring points are adopted.

From a first qualitative look, the results of the electrical surveys showed the expected correlation of decreasing electrical resistivity with the increasing temperature induced by the heat injection, the opposite is true after the source's turning off. The electrical resistivity changed more slowly with increasing distance from the heat source, as temperature did, and resulted dependent upon the water flux conditions within the material. As an average between all the performed tests (both fine and coarse medium), it was observed that a 10% positive variation in temperature generates a 2% – 3% negative change in electrical resistivity. Generally, the heating periods were appreciably monitored by resistivity measurements and the resistivity-derived temperatures are in valid accordance with the numerical model. Conversely, in the cooling periods a slight divergence between temperature and resistivity-derived data is particularly highlighted in Fs and Cd tests (**Fig. 5**), same divergences are also partially noticed in the comparison of temperature and numerical curves (**Fig. 4**). At the same time some heterogeneities appears in some of the presented resistivity-derived temperature maps (particularly in Fs and Cd tests, **Fig. 6** and **9**). These can be related to different phenomena occurring in the medium: (i) evaporation, (ii) chemical reactions induced in the water and (iii) velocity of the water flux.

(i) Evaporation process seems to disturb only when a prolonged heat injection is performed. The resistivity measurements were indeed mainly disturbed in the Fs test, in which a 9 h heat injection was performed, while they were not influenced in other experiments. Evaporation processes, observed on the surface of the box, caused a fictitious increase in resistivity which is not related to the temperature dependence, so that heterogeneities may occur in temperature visualization (**Fig. 6**) and anomalies in the resistivity derived temperature curves (**Fig. 5**). The evaporation process has been quantified by local direct measurements at the end of the test showing a reduction of about 10% water content in a 10 cm zone around the source. This reflect in a more remarkable temperature difference for the sensors located near the source (T1 and T3) than for the farthest ones (T2 and T4). Since the temperature estimation from resistivity data is based on a measured resistivity difference this effect could cause both a lower estimated temperature at the peak and an higher estimated temperature in cool down.

(ii) During the cool down of the same test, data show a return to slightly lower resistivity in respect to the initial condition (higher apparent temperature). This can be attributed to chemical reactions' effect (e.g. mineral dissolution processes occurred in the medium during the heating up). We can hypothesize that the heat injection produces an increase in water TDS (total dissolved solids) that lowers the bulk medium resistivity. As for evaporation, chemical reactions' problem only occurs when a prolonged heat injection is performed; no bias related to this issue is highlighted in other tests. A quantification of this effect was indeed performed during the Fs and Fd tests by measuring fluid resistivity. In Fs test, a value of 22.3 ± 0.1 Ω m was measured in the water squeezed from a sample at the end of the test. Conversely, in the Fd test a value of 22.8 ± 0.1 Ω m was constantly monitored in the water going out of the box after passing through the medium. The initial water resistivity was 22.7 Ω m in both tests. This means that during the conduction + convection test (Fd) no relevant water resistivity variation due to changes in TDS was observed, while an only slight reduction was noted in the pure conduction test (Fs) partially responsible, together with evaporation, of worse data fit. It must be also underlined that the above mentioned water resistivity values were estimated on the whole water volume within the box, smearing possible localized anomalies. It is thus possible that, in limited zones nearby the source, mineral dissolution effect could be more relevant. Generally, we can however say that more specific analyses are necessary in order to evaluate and discern evaporation and chemical reactions influences on resistivity measurements. Divergences here highlighted between registered and resistivity-derived temperatures can be of course related to the action of both processes together.

(iii) Flux velocity, higher in the Cd test, provided worse resistivity-derived temperatures (**Fig. 5**). The rapid change of the flowing water within the box did not allow the heat injection to change the water resistivity in the medium's portions located upstream of the source. Moreover, a slightly higher resistivity is observed after source's turning off, showing a cool down due to the lower temperature of the water flow. The difference of the 2D temperature maps (numerical and resistivity-derived) in this test (**Fig. 10**) also underlines that localized flow paths could be present in the coarser material. These are not reflected in the numerical simulation, which assumes an homogeneous medium, but they are underlined in the resistivity measurements. In the Fd test, in which the flux is slower, heat injection is able to change water resistivity, so the two results are in better agreement. It can be said that resistivity-derived temperature are reliable in the dynamic test with low flux velocity, while they are less trustworthy when a high flux velocity is provided.

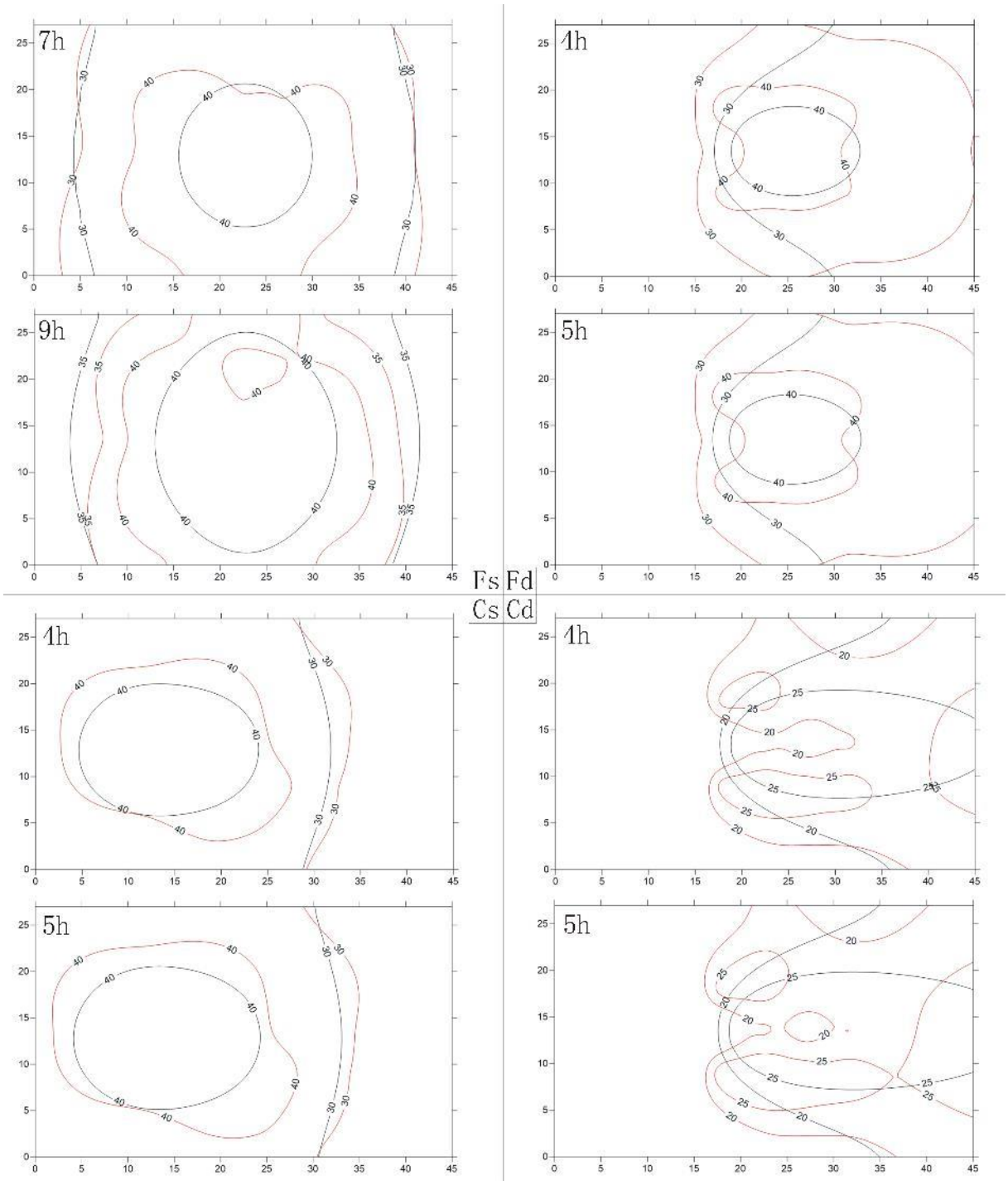

Fig. 10. Comparison between numerical (black lines) and resistivity-derived (red lines) TAZ at isotherms 30 °C and 40 °C for Fs, Fd and Cs; for Cd, isotherms 20 °C and 25 °C were adopted. For all the tests, two steps close to the heating peak are showed.

4. CONCLUSIONS

The present paper presented a series of tests carried out on a laboratory device, build for testing and calibrating the use of electrical apparent resistivity measurements for monitoring the thermal affected zone caused by heat injection. Four examples among the several performed tests were presented. Hourly apparent resistivity measurements were performed on two different porous media in order to image the temperature field within the box. The methodology was supported by numerical simulations calibrated on the temperature recorded by the sensors.

The outcomes of the tests highlighted the reliability of the time-lapse electrical measurements for qualitatively predicting the heat propagation within saturated porous media. The tests showed an acceptable agreement between the TAZ extensions extracted from different approaches (e.g. direct temperature measurements, numerical simulations and apparent resistivity measurements). Radial heat diffusion from the heat source was well described by the variation of apparent resistivity data in tests without flowing water. Tests under flowing water conditions underlined the disturbance of the water flux on the electrical resistivity measurements; the faster the flux velocity, the higher the interference in the collected data. Resistivity measurements appears to reveal more details then simple thermal or thermo-hydraulic modeling. Further studies are however necessary for completely understanding the eventual influence of chemical reactions which occur in a porous medium when a heat injection is provided, particularly at laboratory scale. This could provide a better calibration of resistivity-derived curves in order to be applicable also in field testing.

This study was precursor to what we are planning to do on a living lab prepared at the campus of Torino University in Grugliasco (Giordano et al., 2016; GTES, 2014), where a small ground heat storage system was built. The purpose of this living lab is to replicate at the field scale the laboratory experiments here presented and to serve as a model for further concrete developments of energy saving applications in northern Italy.

REFERENCES

Arato, A., Boaga, J., Comina, C., De Seta, M., Di Sipio, E., Galgaro, A., Giordano, N., Mandrone, G., 2015. Geophysical monitoring for shallow geothermal applications – two Italian case histories. First Break – Near Surface Geoscience 33(8), 75-79.

Arslan, U., Huber H., 2013. Numerical back-analyses of laboratory tests with forced groundwater flow. Proceedings of the Thirty-Eighth Workshop on Geothermal Reservoir Engineering, 1-5.

Bakema, G., Snijders, A.L., Nordell, B., 1995. Underground Thermal Energy Storage, State of the Art Report 1994. Arnhem, The Netherlands, 83 pp.

Bolève, A., Crespy, A., Revil, A., Janod, F., Mattiuzzo, J.L., 2007. Streaming potentials of granular media: Influence of the Duhkin and Reynolds numbers. Journal of Geophysical Research 112, B08204, doi: 10.1029/2006JB004673.

Bonte, M., 2013. Impacts of shallow geothermal energy on groundwater quality: A hydrochemical and geomicrobial study of the effects of ground source heat pumps and aquifer thermal energy storage. Phd Thesis, Gildeprint Enschede, ISBN 978-94-6108-544-3, 175 pp.

Campbell, R.B., Bower, C.A., Richard, L.A., 1948. Change in electrical conductivity with temperature and the relation with osmotic pressure to electrical conductivity and ion concentration for soil extracts. Soil Science Society of America Proceedings 13, 33-69.

Dickinson, J.S., Buik, N., Matthews, M.C., Snijders, A., 2009. Aquifer thermal energy storage: theoretical and operational analysis. Geotechnique 59, 249-260.

Fisch, M.N., Guigas, M., Dalenbäck, J.O., 1998. A review of large-scale solar heating systems in Europe. Solar Energy 63(6), 355-366.

Fragkogiannis, G., Papatheodorou, N., Stamataki, S., 2008. Evaluation of Thermal Performance of Ground - Source Energy Systems. A geophysics supported approach. World Renewable Energy Congress X and Exhibition, July 19th-25th, Glasgow, Scotland.

Friedman, S. P., 2005. Soil properties influencing apparent electrical conductivity: a review. Computers and Electronics in Agriculture 46, 45-70.

Giordano, N., Comina, C., Mandrone, G., Cagni, A., 2016. Borehole thermal energy storage (BTES). First results from the injection phase of a living lab in Torino (NW Italy). Renewable Energy 86, 993-1008, doi: 10.1016/j.renene.2015.08.052.

Hayashi, M., 2004. Temperature-electrical conductivity relation of water for environmental monitoring and geophysical data inversion. Environmental Monitoring and Assessment 96, 119-128, doi: 10.1023/B:EMAS.0000031719.83065.68.

Hayley, K., Bentley, L.R., Gharibi, M., Nightingale. M., 2007. Low temperature dependence of electrical resistivity: Implications for near surface geophysical monitoring. Geophysical Research Letters 34, L18402, doi: 10.1029/2007GL031124.

Hermans, T., Vandenbohede, A., Lebbe, L., Nguyen, F., 2012. A shallow geothermal experiment in a sandy aquifer monitored using electric resistivity tomography. Geophysics 77(1), B11-B21.

Hermans, T., Nguyen, F., Robert, T., Revil, A., 2014. Geophysical methods for monitoring temperature changes in shallow low enthalpy geothermal systems. Energies 7, 5083-5118, doi: 10.3390/en7085083.

Hermans, T., Wildemeersch, S., Jamin, P., Orban, P., Brouyère, S., Dassargues, A., Nguyen, F., 2015. Quantitative temperature monitoring of a heat tracing experiment using cross-borehole ERT. Geothermics 53, 14-26.

Kolditz, O., Bauer, S., Bilke, L., Böttcher, N., Delfs, J.O., Fischer, T., Görke, U.J., Kalbacher, T., Kosakowski, G., McDermott, C.I., Park, C.H., Radu, F., Rink, K., Shao, H.B., Sun, F., Sun, Y.Y., Singh, A.K., Taron, J., Walther, M., Wang, W., Watanabe, N., Wu, Y., Xie, M., Xu, W., Zehner, B., 2012. OpenGeoSys: an opensource initiative for numerical simulation of thermo-hydro-mechanical/chemical (THM/C) processes in porous media, Environmental Earth Science 67, 589-599.

LaBrecque, D.J., Miletto, M., Daily, W., Ramirez, A., Owen, E., 1996. The effects of noise on Occam's inversion of resistivity tomography data. Geophysics 61, 538-548.

Lee, Y., Deming, D., 1998. Evaluation of thermal conductivity temperature corrections applied in terrestrial heat flow studies. Journal of Geophysical Research 103(B2), 2447-2454.

Lo Russo, S., Gnavi, L., Roccia, E., Taddia, G., Verda, V., 2014. Groundwater Heat Pump (GWHP) system modeling and Thermal Affected Zone (TAZ) prediction reliability: Influence of temporal variations in flow discharge and injection temperature. Geothermics 51, 103-112.

Loke, M.H., 2000. Electrical imaging surveys for environmental and engineering studies – A practical guide to 2-D and 3-D surveys. Copyright (1999) M.H. Loke, 67 pp.

Novo, A.V., Bayon, J.R., Castro-Fresno, D., Rodriguez-Hernandez, J., 2010. Review of seasonal heat storage in large basins: Water tanks and gravel-water pits. Applied Energy 87, 390-397.

Paskoy, H.O., Andersson O., Abaci, S., Evliya, H., Turgut, B., 2000. Heating and cooling of a hospital using solar energy coupled with seasonal thermal energy storage in an aquifer. Renewable Energy 19, 117-122.

Rein, A., Hoffman, R., Dietrich, P., 2004. Influence of natural time-dependent variations of electrical conductivity on DC resistivity measurements. Journal of Hydrology 285, 215-232.

Reuss, M., Beuth, W., Schmidt, M., Schoelkopf, W., 2006. Solar district heating with seasonal storage in Attenkirchen. ECOSTOCK 2006, in: 10th International Conference on Thermal Energy Storage, Stockton, USA.

Revil, A., Cathles, L.M., Losh, S., Nunn, J.A., 1998. Electrical conductivity in shaly sands with geophysical applications. Journal of Geophysical Research 103, 23925-23936, doi: 10.1029/98JB02125.

Revil, A., Linde, N., 2006. Chemico-electrochemical coupling in micro-porous media. Journal of Colloid and Interface Science 302, 682-694, doi: 10.1016/j.jcis.2006.06.051.

Robert, T., Hermans, T., Dumont, G., Nguyen, F., Rwabuhungu, D.E., 2013. Reliability of ERT-derived temperature – Insights from laboratory measurements. Near Surface Geoscience, Proceedings of 19th European Meeting of Environmental and Engineering Geophysics, TuS2a10, Bochum, Germany, 9-11 September 2013.

Rosen, M.A., 1999. Second-law analysis of aquifer thermal energy storage systems. Energy 24, 167-182.

Sanner, B., Karytsas, C., Mendrinos, D., Rybach, L., 2003. Current status of ground source heat pumps and underground thermal energy storage in Europe. Geothermics 32, 579-588.

Schmidt, T., Mangold, D., Müller-Steinhagen, H., 2004. Central solar heating plants with seasonal storage in Germany. Solar Energy 76, 165-74.

Slater, L., Binley, A.M., Daily, W., Johnson, R., 2000. Cross-hole electrical imaging of a controlled saline tracer injection. Journal of Applied Geophysics 44, 85-102.

Xu, J., Wang, R.Z., Li, Y., 2014. A review of available technologies for seasonal thermal energy storage. Solar Energy, 103: 610-638.

WEB REFERENCES

DLSC - Drake Landing Solar Community, 2012. Borehole thermal energy storage (BTES) - http://dlsc.ca accessed on September 21

GTES Grugliasco Living Lab, 2014 – www.gtes.unito.it accessed 2015 September 21.

Prof. Andrew Binley, © 2012, Lancaster University - www.es.lancs.ac.uk/people/amb/Freeware/R3t/R3t.htm accessed on 2015 September 21.